Probing the Iron−Substrate Orientation for Taurine/α-Ketoglutarate Dioxygenase Using Deuterium Electron Spin Echo Envelope Modulation Spectroscopy†

Rajendra Bose Muthukumaran,‡ Piotr K. Grzyska,§ Robert P. Hausinger,§,|| and John McCracken*,‡

Department of Chemistry, Department of Microbiology and Molecular Genetics, and Department of Biochemistry and Molecular Biology, Michigan State University, East Lansing, Michigan 48824

Received March 22, 2007

ABSTRACT: The structural relationship between substrate taurine and the non-heme Fe(II) center of taurine/α-ketoglutarate (αKG) dioxygenase (TauD) was measured using electron spin echo envelope modulation (ESEEM) spectroscopy. Studies were conducted on TauD samples treated with NO, cosubstrate αKG, and either protonated or specifically deuterated taurine. Stimulated echo ESEEM data were divided to eliminate interference from ^{1}H and ^{14}N modulations and accentuate modulations from ^{2}H. For taurine that was deuterated at the C_1 position (adjacent to the sulfonate group), ^{2}H ESEEM spectra show features that arise from dipole−dipole and deuterium nuclear quadrupole interactions from a single deuteron. Parallel measurements taken for taurine deuterated at both C_1 and C_2 show an additional ESEEM feature at the deuterium Larmor frequency. Analysis of these data at field positions ranging from $g = 4$ to $g = 2$ have allowed us to define the orientation of substrate taurine with respect to the magnetic axes of the Fe(II)−NO, $S = {}^{3}/_{2}$, paramagnetic center. These results are discussed in terms of previous X-ray crystallographic studies and the proposed catalytic mechanism for this family of enzymes.

The Fe(II)/α-ketoglutarate (αKG)[1] dependent dioxygenases are non-heme, mononuclear iron-containing enzymes that catalyze key reactions in the biosynthesis or biodegradation of a wide range of compounds (*1*). Well-studied examples of this enzyme family include prolyl hydroxylases that function in both collagen biosynthesis (*2*) and intracellular signaling (*3*, *4*), isopenicillin *N* synthase (*5*), and clavaminate synthase (*6*) that produce important antibiotics, TfdA that degrades the herbicide 2,4-dichlorophenoxyacetic acid (*7*, *8*), and AlkB that repairs methylation damage to nucleic acids (*9*, *10*). These enzymes are unified by a common jellyroll or double-stranded β-helix structure (*11*) containing a 2-His-1-carboxylate iron-binding motif (*12*, *13*) with solvent molecules occupying the three remaining coordination sites of the octahedral iron. Oxidative chemistry catalyzed by various family members includes hydroxylation, ring formation, ring expansion, desaturation, and, as only very recently revealed (*14*, *15*), chlorination reactions.

The archetype Fe(II)/αKG hydroxylase is taurine/αKG dioxygenase (TauD), an *Escherichia coli* enzyme that catalyzes the conversion of taurine (2-aminoethanesulfonic acid) to sulfite and aminoacetaldehyde (*16*), as illustrated in Scheme 1. Taurine is found at high concentrations within eukaryotic cells and is a component of the bile salt taurocholate (*17*, *18*). TauD-like enzymes decompose these and other sulfonates, providing an important source of sulfur for many microorganisms (*19*). Because TauD is available in large amounts, highly soluble, and relatively stable, it has been the subject of numerous mechanistic studies (*20*−*29*). Insights gained from studies involving the oxidative chemistry of TauD are likely to apply to many other members of the Fe(II)/αKG dioxygenase family.

A reasonable mechanism of the Fe(II)/αKG hydroxylases is illustrated in Scheme 2. The resting Fe(II) center (**A**) binds the αKG cosubstrate as a chelate, accompanied by dissociation of two water molecules (**B**). Subsequent binding of substrate near the active site is accompanied by dissociation of the last water molecule (**C**), creating a five-coordinate Fe(II) site that is primed to react with oxygen (*30*−*32*). For example, the X-ray crystal structure is known for the anaerobic taurine−αKG−Fe(II)TauD species (*33*, *34*), as shown in Figure 1. The binding of dioxygen leads to an Fe(III)−superoxo or Fe(IV)−peroxo species (**D**) that participates in additional poorly understood chemistry resulting in O−O bond cleavage, decarboxylation of αKG, and formation of an Fe(IV)−oxo intermediate (**E**). This intermediate has been identified in TauD by using a combination of several spectroscopic approaches (*23*−*28*). The Fe(IV)−oxo species is thought to oxidize the substrate by radical rebound-type chemistry (**F**), restoring the ferrous species.

The work described here focuses on the use of advanced electron paramagnetic resonance (EPR) techniques in probing the TauD metallocenter. To convert the $S = 2$ Fe(II) active site into a species that can be studied robustly by these

† These studies were supported by the National Institutes of Health (Grant GM054065 to J.M. and Grant GM063586 to R.P.H.). The National Institutes of Health (RR15880) and the Michigan Economic Development Corp. provided funds for the purchase of our pulse EPR spectrometer.

* To whom correspondence should be addressed.
‡ Department of Chemistry.
§ Department of Microbiology and Molecular Genetics.
|| Department of Biochemistry and Molecular Biology.

[1] Abbreviations: αKG, α-ketoglutarate; TauD, taurine/αKG dioxygenase; ENDOR, electron nuclear double resonance; EPR, electron paramagnetic resonance; ESEEM, electron spin echo envelope modulation; NDO, naphthalene 1,2-dioxygenase; nqi, nuclear quadrupole interaction; ZFS, zero field splitting.

10.1021/bi700562t CCC: $37.00
Published on Web 05/01/2007

Scheme 1

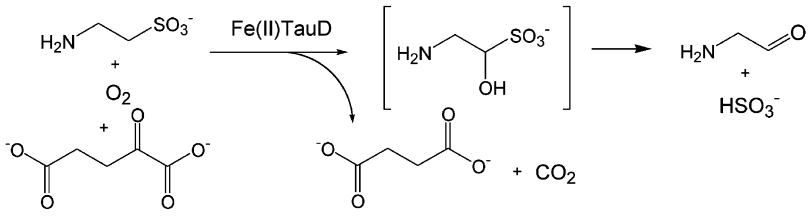

Scheme 2

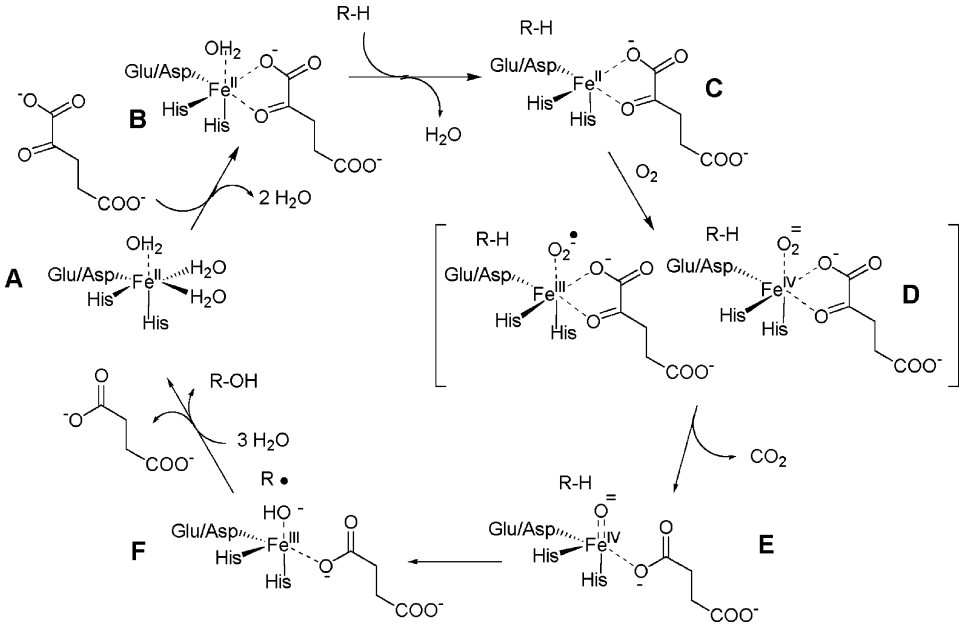

methods, we exploited the known ability of NO, a surrogate of molecular oxygen, to bind to non-heme iron sites and produce an electron spin $S = {}^3/_2$ center (*35*, *36*). Specifically, we examined the NO-bound taurine−αKG−Fe(II)TauD species (with the taurine deuterated on both carbons or on the carbon adjacent to the sulfur atom) by electron spin echo envelope modulation (ESEEM) spectroscopy to measure the distance and relative orientation of the substrate deuterons with respect to the Fe(II)−NO bond. When combined with the results of X-ray crystallographic studies, these spectroscopic results provide a more detailed structure of the catalytic intermediate(s), **D**, in Scheme 2. Because catalysis involves the hydroxylation of a specific C−H bond on substrate taurine, spectroscopic studies that elucidate the structural relationship between Fe and substrate hydrogens provide important details for understanding the enzyme mechanism. These studies with TauD will also provide calibration of this approach for use with related enzymes of unknown structure.

EXPERIMENTAL PROCEDURES

Materials. General chemicals were purchased from Sigma-Aldrich and used without purification. Perdeuterated taurine was obtained from C/D/N Isotopes. An ammonium salt of taurine deuterated at C_1 (the carbon adjacent to the sulfonate group) was a gift from J. C. Price and M. Bollinger and prepared as described previously (*27*).

Enzyme Purification, Assay, and Sample Preparation. Wild-type TauD apoprotein was purified as previously described (*22*). Protein samples and stock solutions of additives were prepared in 25 mM Tris buffer (pH 8.0) and deoxygenated through repeated cycles of air evacuation and flushing with pressurized Ar. Additions were made through sealed septa by using gastight Hamilton syringes. Anaerobic samples were treated with NO by flushing the headspace with the gas, resulting in conversion of the purple αKG−Fe(II)−TauD complexes into a dark yellow species. After approximately 10 s, the excess NO was removed under vacuum and the headspace filled with Ar. All preparative procedures were performed at ambient temperature.

EPR Spectroscopy. Continuous wave and pulsed-EPR data were collected on a Bruker E-680X spectrometer operating at X-band and equipped with a model ER4118-MD-X-5-W1 probe that employs a 5 mm dielectric resonator. The sample temperature was maintained at 4.2 K using an Oxford Instruments liquid helium flow system equipped with a CF-935 cryostat and an ITC-503 temperature controller. ESEEM data were collected using a three-pulse, stimulated echo sequence (90°−τ−90°−T−90°) with 90° microwave pulse widths of 16 ns (full width at half-maximum) and peak powers of 250 W. A four-step phase cycling sequence, ($+x$, $+x$, $+x$), ($-x$, $+x$, $+x$), ($+x$, $-x$, $+x$), ($-x$, $-x$, $+x$), together with the appropriate addition and subtraction of the integrated spin echo intensities served to actively remove the contributions of two-pulse echoes and baseline offsets from the data (*37*). An integration window of 24 ns was used to acquire spin echo amplitudes, and data set lengths were 512 points.

The deuterium contribution to each ESEEM spectrum was elucidated by using the ratio method of Mims together with processing tools available in the Xepr data acquisition and

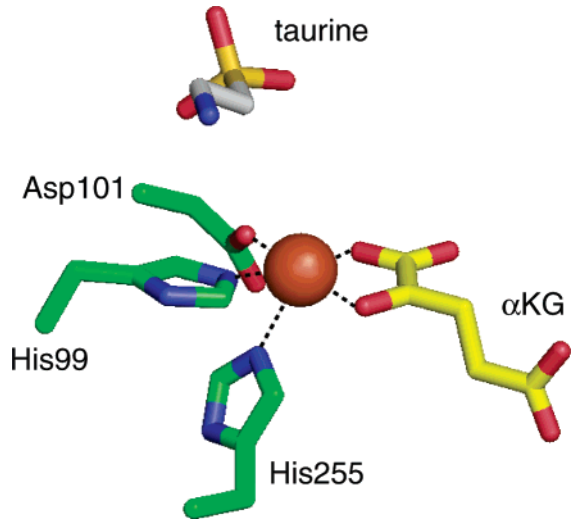

FIGURE 1: TauD active site. The three metal liganding amino acid side chains (His 99, Asp 101, and His 255), the chelated αKG, and the substrate taurine are depicted for monomer A of the four molecules per unit cell in PDB entry 1os7.

processing software provided by Bruker. Specifically, three-pulse ESEEM data collected for enzyme samples prepared with [^{2}H]- and [^{1}H]taurine were normalized by dividing each data set by its maximum amplitude. The normalized ^{2}H ESEEM data were then divided by the corresponding, normalized ^{1}H ESEEM data to obtain a resulting ESEEM pattern dominated by the ^{2}H contribution to the ESEEM. Short phase memory times precluded the use of τ values longer than 200 ns for three-pulse ESEEM, and the use of two-pulse ESEEM data, for the processing of ^{2}H data by using the ratio method (*38*). The time domain data that resulted from this ratio process were tapered with a Hamming window and Fourier transformed (*39*). ESEEM spectra were obtained by taking the absolute value of the real portion of the transforms.

ESEEM simulations of the $I = 1$, deuterium ligand hyperfine couplings were accomplished by using software written in FORTRAN (Absoft). Calculations used the density matrix formalism of Mims to simulate the time domain ESEEM data (*40*, *41*). MATLAB scripts were then used to assemble the simulations according to the product rule (*41*) and to complete the Fourier analysis to obtain simulated ESEEM spectra. The processing and Fourier transformation procedure was identical to that outlined above for the Bruker software. Orientation selection in the ESEEM spectra was identified using the method described by Hoffman and co-workers to integrate the ESEEM response along a contour of a constant effective g value (*42*). A parabolic searching algorithm was used to compute orientations of the Fe(II)−NO center that were resonant at a given field position (*43*).

RESULTS

The electron spin echo (ESE)-detected EPR spectrum of the Fe(II)−NO form of TauD treated with αKG and taurine shows axial symmetry with a $g_\perp$ of 4.00 and a $g_{||}$ of 2.00 (see Figure S1 of the Supporting Information). This observation is typical for Fe(II)−NO complexes and arises from the $M_S = \pm^1/_2$ Kramers doublet of the $S = {}^3/_2$ coupled spin system. The line shape reflects an axially symmetric zero field splitting interaction with its principal axis directed along

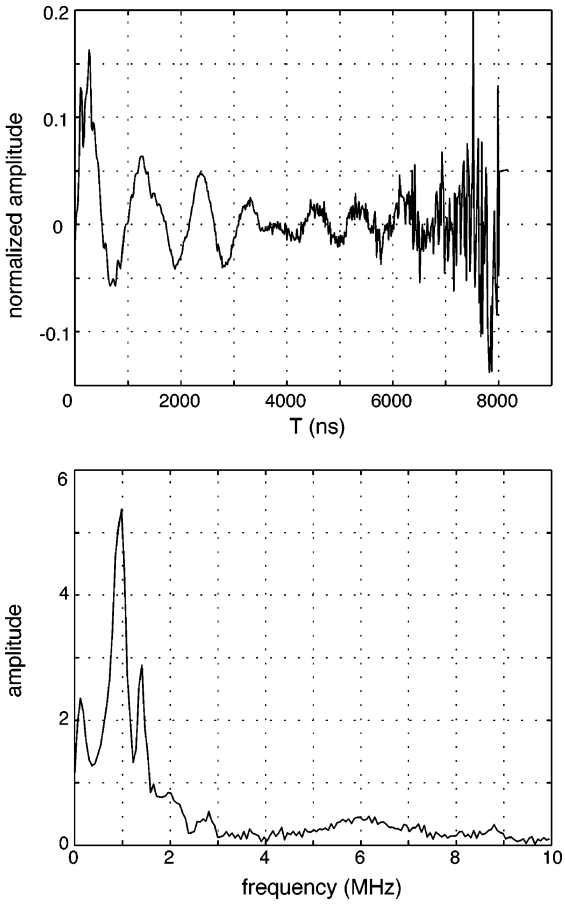

FIGURE 2: Time domain ESEEM ratio (top) and Fourier transform (bottom) generated by dividing time domain ESEEM data obtained for the Fe(II)−NO−TauD species treated with αKG and C_1 [^{2}H]-taurine with data obtained under identical conditions for the Fe(II)−NO−TauD species treated with αKG and taurine. Data sets were normalized to their maximum amplitudes prior to division. A second-degree polynomial was used to remove residual background decay. ESEEM data were collected under the following conditions: microwave frequency, 9.723 GHz; magnetic field strength, 171.0 mT; 90°−τ−90°−T−90° sequence with 16 ns pulses; τ value, 136 ns; T increment, 16 ns; repetition rate, 1 kHz; number of events averaged per time point, 100; scans, four; and sample temperature, 4.2 K.

$g_{||}$ and the Fe(II)−NO bond (*35*). Identical ESE-detected EPR spectra were obtained for Fe(II)−NO TauD treated with αKG and deuterated taurines.

Three-pulse ESEEM spectra were collected at 171.0, 172.8, 190.0, 290.0, 345.0, and 346.0 mT. These spectra were complex, showing contributions from the histidyl ligands, bound NO, and at least two different sets of strongly coupled protons. Two-dimensional ESEEM (HYSCORE) spectra and isotopic substitution studies are being used to assign these peaks, and the results will be the focus of a future publication. A sample three-pulse ESEEM spectrum is shown in the Supporting Information as Figure S2. To reveal the ESEEM contributions from substrate protons, Fe(II)−NO TauD samples treated with αKG and taurine deuterated at C_1 were compared to data collected under identical conditions using protonated taurine. Figure 2 (top) shows the time domain ESEEM contribution of the taurine deuterons at 171.0 mT obtained by dividing the normalized ESEEM data from the C_1 deuterated taurine sample by the normalized ESEEM data collected for the enzyme treated with protonated taurine. The data of Figure 2 show pronounced modulations from

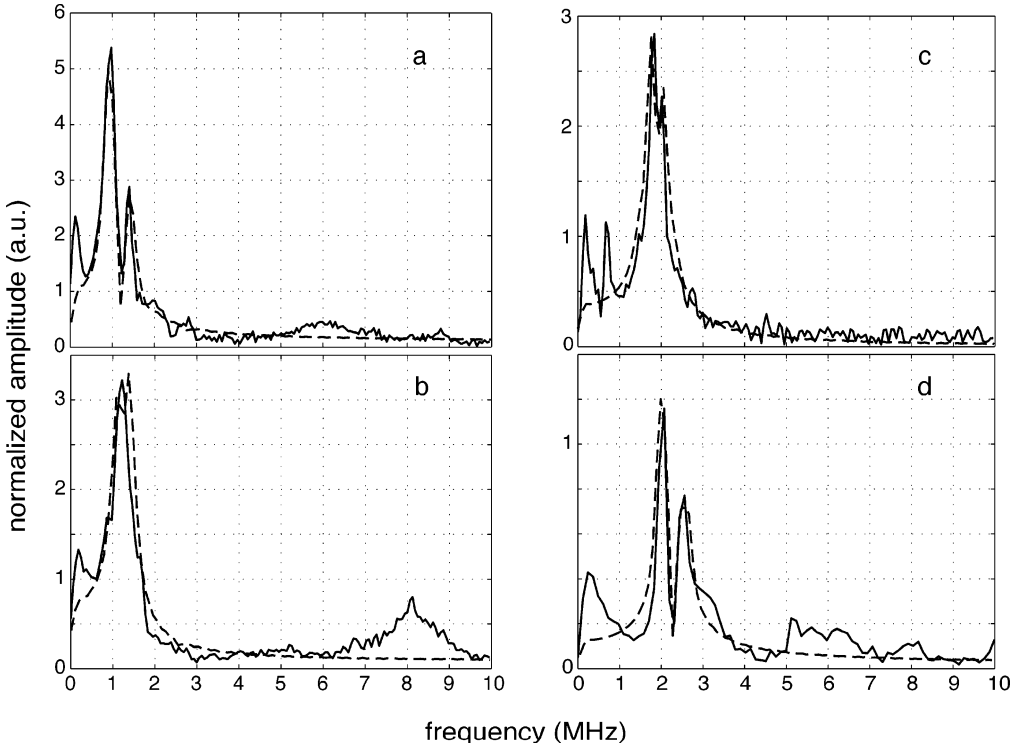

FIGURE 3: Magnetic field dependence of ^{2}H ESEEM spectra (—) obtained for Fe(II)−NO−TauD samples treated with αKG and C_1 [^{2}H]-taurine using the ratio method described for Figure 2. The field positions displayed are (a) 171.0, (b) 190.0, (c) 290.0, and (d) 346.0 mT. Simulations of these ^{2}H ESEEM spectra (− − −) are plotted along with the data. Hamiltonian parameters used for the simulations were as follows: principal g values, 4.0, 4.0, and 2.0; principal deuterium hyperfine values, −0.25, −0.25, and 0.50 MHz; Euler angles for the hyperfine tensor, 0°, 17°, and 0°; e^2qQ, 0.20 MHz; η, 0; and Euler angles relating nqi to hyperfine, 0°, 23°, and 0°.

deuteron hyperfine interactions that have an initial modulation depth of ∼15% of the echo amplitude. For TauD samples, we found that the three-pulse data showed a background decay characterized by an e^{-1} time of ∼2 μs. This led to substantial noise in the ratio data at longer times and often required that a first- or second-order polynomial fit be used to correct the baseline. The absolute value spectrum obtained after applying a Hamming window and cosine Fourier transform to the ESEEM ratio revealed ESEEM frequencies at 0.95 and 1.39 MHz that could be assigned to the C_1 deuterons of taurine [Figure 2 (bottom)].

Figure 3 shows the ^{2}H ESEEM spectra that result from repeating the measurement and processing procedure described for Figure 2 at 190.0 mT (Figure 3b), 290.0 mT (Figure 3c), and 346.0 mT (Figure 3d). Figure 3a shows that in the $g_\perp$ region, a pair of ESEEM frequencies at 0.95 and 1.39 MHz is observed. These coalesce to a single broad feature centered at 1.2 MHz at 190.0 mT (Figure 3b) and begin to split again at 290.0 mT (Figure 3c) where ^{2}H ESEEM components at 1.8 and 2.0 MHz are resolved. When $g = 2.0$ at 346.0 mT (Figure 3d), where one samples orientations of the enzyme with the laboratory magnet field nearly parallel to the principal axis of the zero field splitting (ZFS) interaction, the ^{2}H ESEEM spectrum exhibits two well-resolved peaks at 2.0 and 2.5 MHz. Further examination of Figure 3 reveals other frequencies in the ratio data. Specifically, a minor peak at 0.2 MHz is found in all of the spectra, and we have attributed it to the baseline processing and windowing procedure used to process the data. The broad ESEEM peaks centered at 6.0 and 8.1 MHz for the spectra taken at 171 (Figure 3a) and 190 mT (Figure 3b), respectively, are likely due to protons and may reflect the proton difference portion of our study. The narrow peak at 0.7 MHz resolved in the 290 mT ratio (Figure 3c) and the broad features that range from 5 to 7 MHz for the 346 mT data (Figure 3d) are likely due to ^{14}N ESEEM that is not fully compensated by the data division procedure. Approximations that stem from the data division procedure used to obtain the data presented in Figures 2−4 have been discussed in detail elsewhere (*44*).

Figure 4 shows ^{2}H ESEEM data for Fe(II)−NO TauD treated with αKG and taurine deuterated at both C_1 and C_2 positions. Figure 4a shows data collected in the g-perpendicular region at 172.8 mT where three ^{2}H ESEEM components at 0.9, 1.1, and 1.3 MHz are now resolved. A comparison of these data to data collected at 171.0 mT for the C_1 deuterated taurine sample showed that addition of two deuterons at C_2 served to add a new ESEEM feature at 1.1 MHz, the Larmor frequency of deuterium at this magnetic field strength. The ^{2}H ESEEM spectra of panels b and c of Figure 4 are dominated by a single, broad peak centered at the deuterium Larmor frequencies of 1.2 MHz (190 mT, Figure 4b) and 1.9 MHz (290 mT, Figure 4c), respectively. A comparison of the data of Figures 3b and 4b shows that the amplitude of the peak at 1.2 MHz increases for the perdeuterated taurine sample, indicating that addition of deuterons to the C_2 position of the substrate also serves to add an additional feature at the deuterium Larmor frequency. Similar conclusions can be made from comparing the ^{2}H ESEEM data of panels c and d of Figure 4 with those of panels c and d of Figure 3. For both cases, addition of the C_2 deuterons to taurine yields extra ESEEM intensity at the deuterium Larmor frequencies of 1.9 MHz (290 mT) and 2.25 MHz (346 mT).

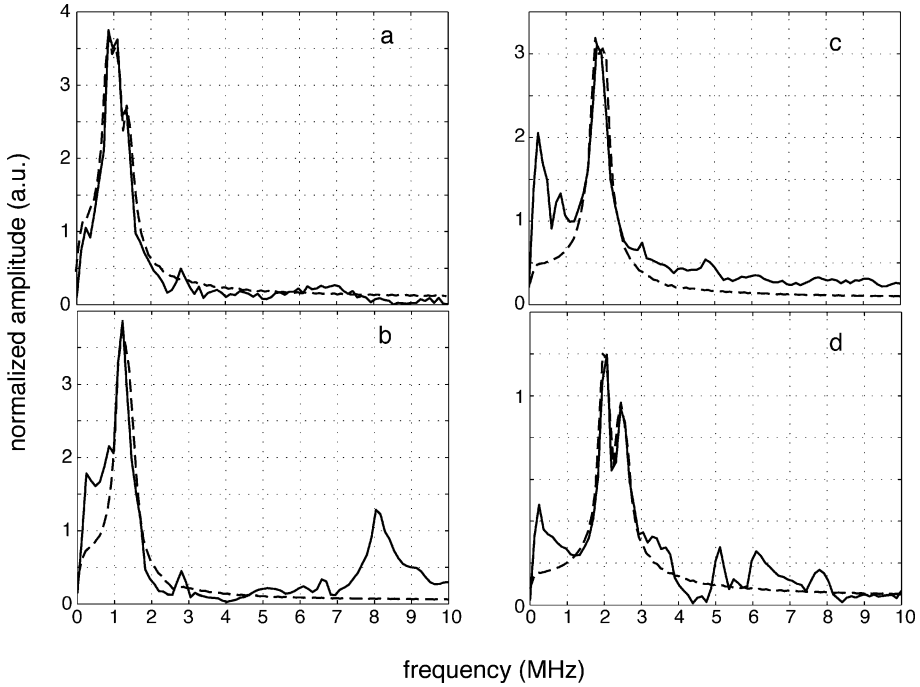

FIGURE 4: Magnetic field dependence of ^{2}H ESEEM spectra obtained for Fe(II)−NO−TauD samples treated with αKG and taurine deuterated at both C_1 and C_2. Data were obtained using the ratio method described for Figure 3. The field positions displayed are (a) 172.8, (b) 190.0, (c) 290.0, and (d) 345.0 mT. Simulated ^{2}H ESEEM spectra for the C_1 and C_2 deuterated taurine are plotted along with the data (− − −). For the stronger coupled C_1 deuteron, Hamiltonian parameters identical to those in Figure 3 were used. Hamiltonian parameters used for a second deuteron on C_2 were as follows: principal deuterium hyperfine values, −0.13, −0.13, and 0.26 MHz; Euler angles for the hyperfine tensor, 0°, 63°, and 0°; e^2qQ, 0.20 MHz; η, 0; and Euler angles relating nqi to hyperfine, 0°, 23°, and 0°.

Analysis. Analysis of these ^{2}H ESEEM data to determine the hyperfine parameters and the number of contributing nuclei was accomplished by spectral simulation. The spin Hamiltonian used to model the deuterium ligand hyperfine interaction consisted of nuclear Zeeman, electron−nuclear hyperfine, and nuclear quadrupole terms. The simulation software computes ESEEM patterns using the approach described in Experimental Procedures. Because the microwave pulses used in our experiments have a finite bandwidth, ESEEM patterns were calculated over a 4 mT width of magnetic field strengths centered about the experimental field value with each discrete ESEEM pattern weighted according to a Gaussian distribution (e^{-1} width of 2 mT). Deuterium hyperfine and nuclear quadrupole tensors were transformed into the **g** tensor axis system at the start of the calculation, and the resonance conditions, magnetic field setting and microwave frequency, were used to compute orientations of the magnetic axes that contributed to the ESEEM. Orientation averaging was accomplished by converting the line integral about the constant effective g value to a definite integral over ϕ where the integrating factors are determined numerically (*42*).

In an attempt to directly measure the deuterium quadrupole coupling parameters for taurine deuterated at the C_1 position, four-pulse ESEEM measurements were undertaken. In four-pulse experiments, the ESEEM spectrum features additional peaks at the sum combination frequencies of the fundamental hyperfine frequencies resolved in the three-pulse ESEEM experiment. For deuterons, the sum combination peaks should yield a pair of frequencies separated by the deuterium nuclear quadrupole coupling constant and the details of the nqi tensor orientation with respect to the **g** tensor (*45*, *46*). These measurements were problematic for our samples because the data division procedure described above for our three-pulse ESEEM experiments was not able to eliminate ^{14}N and ^{1}H ESEEM contributions to the data that serve to mask the deuterium sum combination frequency. This difficulty is likely a consequence of the overlap of three- and four-pulse echoes in these experiments that cannot be separated by phase cycling. Fortunately, we found that for four-pulse ESEEM data collected at higher fields, 290.0 and 346.0 mT, a clean spectral window was realized in the region of the deuterium sum combination peak (Figure S3 of the Supporting Information). However, the deuterium sum combination peak resolved at both of these magnetic field positions was featureless and centered at twice the Larmor frequency of deuterium. This poor resolution was a result of the damping time observed for the four-pulse study, which was on the order of 0.5 μs for the data collected at 290 mT (see Figure S3).

For simulation of the ^{2}H ESEEM data of Figure 3, we sought to determine a set of spin Hamiltonian parameters that would reproduce the frequencies, relative amplitudes, and initial modulation depths of the data. Furthermore, a single set of Hamiltonian parameters should be able to account for the data obtained at each field position that was studied. For our calculations, the nuclear quadrupole coupling constant, e^2qQ, was fixed at 0.2 MHz and the asymmetry parameter, η, was set to zero on the basis of literature values from nuclear quadrupole resonance studies (*47*). Because the deuterium hyperfine interaction is expected to be a through-space interaction [substrate taurine is not bound to the Fe(II)−NO center], the isotropic hyperfine coupling was set to zero and the hyperfine tensor was fixed to axial symmetry. In practice, these hyperfine couplings must be scaled to their effective values using the ratio of the appropriate effective

g value that describes the EPR signal within the $M_S = \pm^1/_2$ doublet of this $S = {}^3/_2$ spin system with the free electron *g* value, 2.00 (*48*, *49*). Examination of the C_1 ^{2}H ESEEM data (Figure 4, solid lines) shows that a pair of frequencies separated by 0.4 and 0.5 MHz is resolved at both $g_\perp$ and $g_{||}$, respectively. Because the effective *g* value doubles as you go from $g_{||}$ to $g_\perp$, the experimental results lead one immediately to the conclusion that the deuteron giving rise to the ESEEM is oriented close to $g_{||}$ or the principal axis of the ZFS tensor.

Computer simulations of the C_1 ^{2}H ESEEM spectra are shown with dashed lines in Figure 3 for the four field positions that were studied. Except for the details of the line shape resolved at 190 mT, these simulations faithfully reproduce the observed ESEEM frequencies, relative amplitudes, and modulation intensities, or depths. Because of the axial symmetry of **g**, hyperfine, and nuclear quadrupole tensors, the simulations were sensitive only to the "*y*′ rotation" of the Euler angle rotation schemes that were used to relate the deuterium hyperfine tensor to the **g** tensor and the nuclear quadrupole tensor to the hyperfine tensor (*50*). The deuterium peak frequency separations at 171 mT (Figure 3a) and 346 mT (Figure 3d) were best simulated by an electron−nuclear dipolar interaction of 0.30 ± 0.05 MHz, and a colatitude with respect to the $g_{||}$ axis of 20 ± 3°. The angle describing the relative orientation of the deuterium hyperfine and nuclear quadrupole principal axes was 23 ± 3°. This range of hyperfine couplings corresponds to a range of dipole−dipole distances (based on our reference *g* value of 2.00) of 3.4 ± 0.2 Å. We accounted for the modulation depths by considering that only one of the C_1 deuterons contributed to the observed ^{2}H ESEEM.

Computer simulations of the ^{2}H ESEEM spectra obtained for the samples with both taurine carbons deuterated are shown as dashed lines in Figure 4. The addition of deuterons to C_2 serves to add a feature centered at the Larmor frequency of deuterium to the ESEEM data obtained at the four magnetic field positions displayed in Figure 4. At $g_\perp$, 172.8 mT (Figure 4a), this feature is clearly resolved, while at the other three field strengths, the addition of this "matrix" ESEEM component manifests itself in an apparent decrease in spectral resolution. The requirement that ^{2}H ESEEM data be resolved at the Larmor frequency across the entire Fe(II)−NO EPR spectrum placed an upper limit on the value of the axial hyperfine coupling strength, while the amplitude of this spectral feature at each field position placed restrictions on both the deuterium hyperfine coupling strength and a colatitude angle that describes the relative orientations of $g_{||}$ and the hyperfine principal axis. For the simulations depicted in Figure 4, a dipolar hyperfine coupling strength of 0.13 MHz and an angle of 63° between $g_{||}$ and the hyperfine principal axis were used. Application of the dipole−dipole model to the 0.13 MHz hyperfine field yields a distance of 4.5 Å for this weaker interaction. The simulations of Figure 4 yield initial modulation depths of 14, 19, 11, and 5% for spectra (dashed lines) in panels a−d of Figure 4, respectively. These agree well with experimental values for the data of Figure 4 (solid lines) which were 17, 20, 12, and 6%, respectively. These simulations were not sensitive to the nuclear quadrupole coupling parameters of the weaker coupled deuteron, so the value of the angle between the hyperfine and quadrupole principal axes was fixed at the value obtained for analysis of the stronger coupling.

Only one C_2 deuteron was considered in the calculations discussed above and summarized in Figure 4. Because the addition of two deuterons to C_2 resulted in only the addition of a single spectral feature to the data, it is possible that both C_2 deuterons contribute to the ESEEM. The X-ray crystallographic data (Figure 1) indicate that both deuterons on C_2 would be directed away from the open coordination site on the Fe where NO is likely bound. Computer simulations of the ESEEM arising from both C_2 deuterons yielded an average dipolar coupling strength of 0.09 ± 0.005 MHz and an angle between $g_{||}$ and a hyperfine tensor principal axis of 63 ± 5°. These are "average " values as only one set of hyperfine parameters were used together with the spherical model approximation to the product rule to obtain simulations comparable to those in Figure 4 (*51*). The anisotropic hyperfine coupling range determined above translates to a dipole−dipole distance of 5.1 ± 0.2 Å if a reference *g* value of 2.00 is used.

DISCUSSION

A detailed description of the electronic structure of the Fe(II)−NO model complexes and other non-heme iron dioxygenases has shown that the paramagnetic center giving rise to the EPR spectrum (Figure S1 of the Supporting Information) is best described as a high-spin Fe(III) $S = {}^5/_2$ ion antiferromagnetically coupled to an $S = 1$, NO^- ligand (*35*). Furthermore, Brown et al. point out that the lack of ligand hyperfine coupling and the anisotropy observed in the ^{57}Fe hyperfine coupling of Fe(II)−NO model complexes and the extradiol dioxygenases (*52*) show that the paramagnetism of this center is best described by a model in which the two unpaired electrons on the NO^- ligand are spin paired with unpaired spins in the Fe d_{xz} and d_{yz} orbitals, leaving the remaining three, unpaired 3d electrons to account for the $S = {}^3/_2$ spin state. As noted above, the large zero field splitting interaction observed for these complexes gives rise to an EPR spectrum due to the $M_s = \pm^1/_2$ Kramers doublet. If the electron spin Hamiltonian is taken to consist of an axial ZFS term and an isotropic electronic Zeeman term with a *g* of 2.00, it can be shown that the resulting EPR spectrum will range from $g = 2.00$, when the laboratory magnetic field is directed along the principal axis of the ZFS interaction, to $g = 4.00$, when the field is directed perpendicular to the principal axis of the ZFS tensor (*35*).

This quantum mechanical model for the Fe−NO EPR spectrum was used by Yang et al. to interpret ligand hyperfine couplings resolved in ^{2}H electron nuclear double-resonance (ENDOR) experiments for substrate naphthalene bound to Fe(II)−NO naphthalene 1,2-dioxygenase (NDO). These authors used a point dipole−dipole model to extract Fe−^{2}H distances from the ^{2}H hyperfine coupling aniosotropy and used tensor axis orientations to define the location of these coupled deuterons with respect to the Fe−N(O) bond axis (*48*). Using an identical picture for the paramagnetic center, the dipole−dipole distances determined from analysis of our ESEEM spectra can be summarized as described in the legend of Figure 5. Specifically, ESEEM results for taurine deuterated at the C_1 position are best described by a single deuteron that is 3.4 ± 0.2 Å from the iron atom and

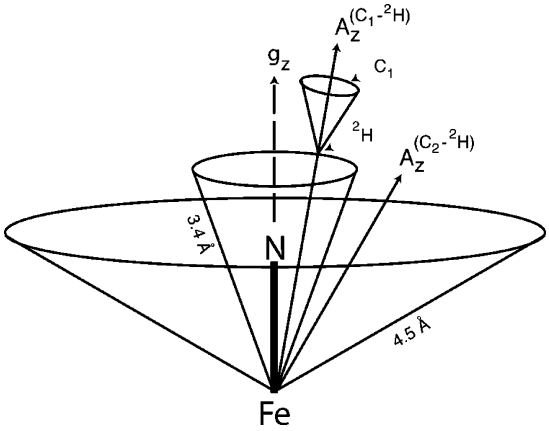

FIGURE 5: Schematic drawing of the geometrical relationship between the coupled deuterons at the C_1 and C_2 positions of taurine and the $g_{||}$ axis, co-incident with the Fe−N(O) bond.

lies on a cone that makes a 20 ± 3° angle with the unique axis of the ZFS interaction, or the Fe(III)−NO^- bond axis. For perdeuterated taurine, an additional deuterium ESEEM interaction could be described by including a second deuteron, positioned 4.5 ± 0.2 Å from the iron on a cone that makes a 63 ± 5° angle with the Fe−N(O) bond axis, in our simulations. Alternatively, both C_2 deuterons could be responsible for this weaker interaction showing an average distance of 5.1 Å from the Fe and also positioned on a cone making a 63° angle with the Fe−N(O) bond axis.

These results are similar to those reported from ^2H ENDOR studies on the Fe(II)−NO adduct of NDO where the C_1 and C_2 deuterons of substrate naphthalene were found 4.3 and 5.0 Å from the Fe atom, respectively. The principal axis of the hyperfine tensor for the C_1 deuteron of substrate naphthalene made a 10° angle with the Fe−NO bond axis. For NDO, X-ray crystallographic analysis of reduced forms of the protein prepared with naphthalene and oxygen shows distances from iron to C_1 and C_2 of naphthalene of ∼4 Å. This would place the naphthalene deuterons bound to these carbons 3−4 Å from the iron, distances somewhat shorter than what was found in the ENDOR studies, but in good agreement with the distance reported here for the proximal C_1 deuteron of substrate taurine (*53*). If one takes the Fe−N bond length for the NO ligand to be 1.8 Å, commensurate with X-ray absorbance fine structure spectroscopic results on FeEDTA-NO (*35*), the proximal C_1 deuteron of taurine will be positioned 1.8 Å from the nitrogen of the bound NO group. The angle defining the orientation of the Fe−N(O) bond with the coupled C_1 deuteron of taurine (20 ± 3°) is somewhat wider than that measured for the C_1 naphthalene deuteron of reduced NDO by ENDOR (10°) or estimated from X-ray crystallography on that enzyme (∼13°) (*48*). These differences in substrate deuteron (proton) distances and orientations are modest given the different catalytic functions and cosubstrate requirements of TauD and NDO. In both cases, the measured deuterium hyperfine couplings provide metrical information that is commensurate with the substrate C−H bond(s) to be hydroxylated.

In our analysis of the ^2H ESEEM data obtained from Fe(II)−NO−TauD samples treated with taurine deuterated at C_1, we considered only the contributions of the proximal deuteron (Figure 3). The nuclear quadrupole interaction (nqi) for the stronger coupled deuteron is axial, with the principal axis of the nqi tensor directed along the C_1-^2H bond. In our simulations, we found that the principal axis of the nqi made a 23 ± 3° angle with the principal axis of the deuterium hyperfine tensor. Taking the C_1-^2H bond length to be 1 Å, we can place a third cone in Figure 5 at the position of the proximal C_1 deuteron to mark the locus of positions for C_1 of taurine. Taking the bonding about C_1 to be sp^3 hybridized and the $^2H-C-^2H$ bond angle to be 109°, we find the distal C_1 deuteron will lie ∼5 Å from the iron. The resulting dipolar hyperfine coupling for this deuteron will give rise to weak ESEEM as the modulation intensities are inversely proportional to the dipole−dipole distance raised to the sixth power (*51*). The contributions of the distal deuteron to the ESEEM spectra of Figures 2 and 3 would be centered at the deuterium Larmor frequency. The best chance of seeing this contribution would be at $g = 2$ for the C_1-deuterated taurine sample (Figure 3d) where there is a fairly clean window in the ESEEM spectrum. Simulations of the ^2H ESEEM for these conditions that consider a dipole−dipole distance of 5.0 Å and an angle of 11° between the Fe−N(O) bond axis and the principal axis of the ^2H hyperfine tensor predict a modulation depth or intensity of 0.5%. Because the modulations due to the stronger coupled deuteron, characterized by a 3.4 Å dipole−dipole distance, are about 6% at $g = 2$, we conclude that the ESEEM from the distal C_1 deuteron is too weak to resolve in our experiments. This decreased modulation depth for the distal C_1 deuteron stems from its increased dipolar distance and its orientation close to the Fe−N(O) or $g_{||}$ axis where integrating factors in the orientation averaging are small.

Taken together, the relative contributions of the two C_1 deuterons to the ESEEM and the intermediate contribution of one or both of the C_2 deuterons provide important details about how substrate taurine is positioned for specific hydroxylation of C_1 and the subsequent harvesting of sulfite. Considering NO to be a reasonable surrogate for O_2^{2-} or $O_2^{-\bullet}$ in Scheme 2 (species **D**), our ESEEM measurements show that one of the C_1 deuterons is positioned 3.4 Å from the Fe at an angle with respect to the Fe−N(O) axis that would result in the distance to the NO nitrogen atom being 1.8 Å. Because the other C_1 deuteron does not contribute to the ESEEM, C_1 must be oriented so that this second deuteron is directed away from the nitrogen of the NO group and close to the $g_{||}$ axis. The larger angle and distance needed to describe the location of the C_2 deuteron(s) likely show that substrate taurine has been oriented to position the C_2-H bonds so they are not able to react with the Fe(IV)−oxo species thought to trigger the C−H bond hydroxylation chemistry (Scheme 2, **E**).

To compare our ESEEM results with the X-ray structure (*34*), the most recent TauD structure was downloaded from the PDB and the program Refmac was used to model protons onto the carbon framework of substrate taurine. Because the X-ray results are from crystals grown anaerobically, the NO ligand was modeled into the crystal structure by using bond lengths and angles from model compound studies (*35*) and by placing the Fe−N(O) bond 180° from the "axial" Fe−N(histidine) bond. The results show that the proximal C_1 proton is 3.0 Å from the Fe atom and makes a 32° angle with the Fe−N(O) bond while the closest C_2 proton is 4.4 Å from the Fe and makes an angle of 52° with the Fe−N(O) bond. Given that there could easily be a 10° error in

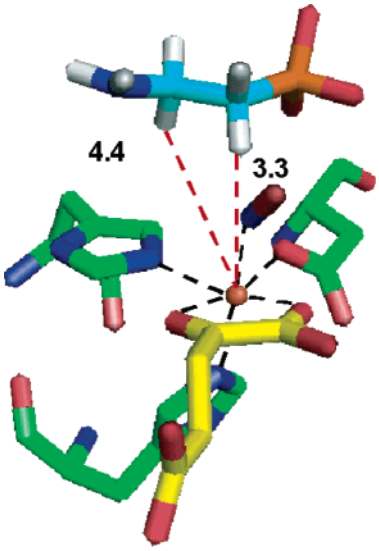

FIGURE 6: Structure of the TauD active site as taken from monomer A of the four molecules per unit cell in PDB entry 1os7. The taurine protons and NO ligand were modeled into the structure using Refmac. The carbon framework of taurine was rotated slightly from the structure supplied to the Protein Data Bank (Figure 1) to achieve Fe−proton distances of 3.3 Å for the C_1 proximal proton and 4.4 Å for the closest C_2 proton.

the orientation of the Fe−N(O) bond axis, one can easily justify moving the Fe−N(O) bond to match the corresponding angles from our ESEEM measurements (Figure 5). In addition, the low resolution of this structure and, more specifically, the taurine electron density map readily allow for modest reorientation of the taurine carbon framework. Figure 6 shows the results of these modest adjustments of the crystal structure and provides a structure that is in excellent agreement with our ESEEM results.

ACKNOWLEDGMENT

We thank J. C. Price and Marty Bollinger for the deuterated taurine labeled at the C_1 position and Tina Müller for providing Figure 1. We also thank James H. Geiger for advice and discussions concerning the X-ray crystallographic structures of TauD and for helping with the comparison shown in Figure 6.

SUPPORTING INFORMATION AVAILABLE

ESE-detected EPR spectrum of the Fe(II)−NO−TauD species treated with αKG and taurine (Figure S1), an example three-pulse ESEEM data set for the Fe(II)−NO−TauD species showing both time domain data and its corresponding ESEEM spectrum (Figure S2), and four-pulse ESEEM data and spectrum collected for the Fe(II)−NO−TauD species treated with αKG and taurine (Figure S3). This material is available free of charge via the Internet at http://pubs.acs.org.

REFERENCES

1. Hausinger, R. P. (2004) Fe(II)/α-ketoglutarate-dependent hydroxylases and related enzymes, *Crit. Rev. Biochem. Mol. Biol. 39*, 21−68.
2. Kivirikko, K. I., and Pihlajaniemi, T. (1998) Collagen hydroxylases and the protein disulfide isomerase subunit of prolyl 4-hydroxylase, *Adv. Enzymol. Relat. Areas Mol. Biol. 72*, 325−398.
3. Schofield, C. J., and Radcliffe, P. J. (2004) Oxygen sensing by hydroxylases, *Nat. Rev. Mol. Cell Biol. 5*, 343−354.
4. Schofield, C. J., and Ratcliffe, P. J. (2005) Signalling hypoxia by HIF hydroxylases, *Biochem. Biophys. Res. Commun. 338*, 617−626.
5. Roach, P. L., Clifton, I. J., Fülöp, V., Harlos, K., Barton, G. J., Hajdu, J., Andersson, K., Schofield, C. J., and Baldwin, J. E. (1995) Crystal structure of isopenicillin *N* synthase is the first from a new structural family of enzymes, *Nature 375*, 700−704.
6. Zhang, Z., Ren, J., Stammers, D. K., Baldwin, J. E., Harlos, K., and Schofield, C. J. (2000) Structural origins of the selectivity of the trifunctional oxygenase clavaminic acid synthase, *Nat. Struct. Biol. 7*, 127−133.
7. Fukumori, F., and Hausinger, R. P. (1993) Purification and characterization of 2,4-dichlorophenoxyacetate/α-ketoglutarate dioxygenase, *J. Biol. Chem. 268*, 24311−24317.
8. Hogan, D. A., Smith, S. R., Saari, E. A., McCracken, J., and Hausinger, R. P. (2000) Site-directed mutagenesis of 2,4-dichlorophenoxyacetic acid/α-ketoglutarate dioxygenase. Identification of residues involved in metallocenter formation and substrate binding, *J. Biol. Chem. 275*, 12400−12409.
9. Falnes, P. O., Johansen, R. F., and Seeberg, E. (2002) AlkB-mediated oxidative demethylation reverses DNA damage in *Escherichia coli*, *Nature 419*, 178−182.
10. Trewick, S. C., Henshaw, T. F., Hausinger, R. P., Lindahl, T., and Sedgwick, B. (2002) Oxidative demethylation by *Escherichia coli* AlkB directly reverts DNA base damage, *Nature 419*, 174−178.
11. Clifton, I. J., McDonough, M. A., Ehrismann, D., Kershaw, N. J., Granatino, N., and Schofield, C. J. (2006) Structural studies on 2-oxoglutarate oxygenases and related double-stranded *β*-helix fold protein, *J. Inorg. Biochem. 100*, 644−669.
12. Hegg, E. L., and Que, L., Jr. (1997) The 2-His-1-carboxylate facial triad, *Eur. J. Biochem. 250*, 625−629.
13. Costas, M., Mehn, M. P., Jensen, M. P., and Que, L., Jr. (2004) Dioxygen activation at mononuclear nonheme iron active sites: Enzymes, models, and intermediates, *Chem. Rev. 104*, 939−986.
14. Vaillancourt, F. H., Yeh, E., Vosburg, D. A., O'Conner, S. E., and Walsh, C. T. (2005) Cryptic chlorination by a non-haem iron enzyme during cyclopropyl amino acid biosynthesis, *Nature 436*, 1191−1194.
15. Vaillancourt, F. H., Yin, J., and Walsh, C. T. (2005) SyrB2 in syringomycin E biosynthesis is a nonheme Fe^{II} α-ketoglutarate- and O_2-dependent halogenase, *Proc. Natl. Acad. Sci. U.S.A. 102*, 10111−10116.
16. Eichhorn, E., van der Ploeg, J. R., Kertesz, M. A., and Leisinger, T. (1997) Characterization of α-ketoglutarate-dependent taurine dioxygenase from *Escherichia coli*, *J. Biol. Chem. 272*, 23031−23036.
17. Huxtable, R. J. (1992) Physiological actions of taurine, *Physiol. Rev. 72*, 101−163.
18. Schuller-Lewis, G. B., and Park, E. (2003) Taurine: New implications for an old amino acid, *FEMS Microbiol. Lett. 226*, 195−202.
19. Kertesz, M. A. (1999) Riding the sulfur cycle: Metabolism of sulfonates and sulfate esters in Gram-negative bacteria, *FEMS Microbiol. Rev. 24*, 135−175.
20. Ryle, M. J., Koehntop, K. D., Liu, A., Que, L., Jr., and Hausinger, R. P. (2003) Interconversion of two oxidized forms of TauD, a non-heme iron hydroxylase: Evidence for bicarbonate binding, *Proc. Natl. Acad. Sci. U.S.A. 100*, 3790−3795.
21. Ryle, M. J., Liu, A., Muthukumaran, R. B., Ho, R. Y. N., Koehntop, K. D., McCracken, J., Que, L., Jr., and Hausinger, R. P. (2003) O_2- and α-ketoglutarate-dependent tyrosyl radical formation in TauD, an α-keto acid-dependent non-heme iron dioxygenase, *Biochemistry 42*, 1854−1862.
22. Ryle, M. J., Padmakumar, R., and Hausinger, R. P. (1999) Stopped-flow kinetic analysis of *Escherichia coli* taurine/α-ketoglutarate dioxygenase: Interactions with α-ketoglutarate, taurine, and oxygen, *Biochemistry 38*, 15278−15286.
23. Price, J. C., Barr, E. W., Glass, T. E., Krebs, C., and Bollinger, J. M., Jr. (2003) Evidence for hydrogen abstraction from C1 of taurine by the high-spin Fe(IV) intermediate detected during oxygen activation by taurine:α-ketoglutarate dioxygenase (TauD), *J. Am. Chem. Soc. 125*, 13008−13009.
24. Price, J. C., Barr, E. W., Tirupati, B., Bollinger, J. M., Jr., and Krebs, C. (2003) The first direct characterization of a high-valent iron intermediate in the reaction of an α-ketoglutarate-dependent dioxygenase: A high-spin Fe(IV) complex in taurine/α-ketoglutarate dioxygenase (TauD) from *Escherichia coli*, *Biochemistry 42*, 7497−7508.

25. Proshlyakov, D. A., Henshaw, T. F., Monterosso, G. R., Ryle, M. J., and Hausinger, R. P. (2004) Direct detection of oxygen intermediates in the non-heme Fe enzyme taurine/α-ketoglutarate dioxygenase, *J. Am. Chem. Soc. 126*, 1022−1023.
26. Riggs-Gelasco, P. J., Price, J. C., Guyer, R. B., Brehm, J. H., Barr, E. W., Bollinger, J. M., Jr., and Krebs, C. (2004) EXAFS spectroscopic evidence for an Fe=O unit in the Fe(IV) intermediate observed during oxygen activation by taurine:α-ketoglutarate dioxygenase, *J. Am. Chem. Soc. 126*, 8108−8109.
27. Price, J. C., Barr, E. W., Hoffart, L. M., Krebs, C., and Bollinger, J. M., Jr. (2005) Kinetic dissection of the catalytic mechanism of taurine:α-ketoglutarate dioxygenase (TauD) from *Escherichia coli*, *Biochemistry 44*, 8138−8147.
28. Grzyska, P. K., Ryle, M. J., Monterosso, G. R., Liu, J., Ballou, D. P., and Hausinger, R. P. (2005) Steady-state and transient kinetic analyses of taurine/α-ketoglutarate dioxygenase: Effects of oxygen concentration, alternative sulfonates, and active site variants on the Fe(IV) intermediate, *Biochemistry 44*, 3845−3855.
29. Kalliri, E., Grzyska, P. K., and Hausinger, R. P. (2005) Kinetic and spectroscopic investigation of Co^{II}, Ni^{II}, and *N*-oxalylglycine inhibition of the Fe^{II}/α-ketoglutarate dioxygenase, TauD, *Biochem. Biophys. Res. Commun. 338*, 191−197.
30. Pavel, E. G., Kitajima, N., and Solomon, E. I. (1998) Magnetic circular dichroism spectroscopic studies of mononuclear non-heme ferrous model complexes. Correlation of excited- and ground-state electronic structure with geometry, *J. Am. Chem. Soc. 120*, 3949−3962.
31. Zhou, J., Kelly, W. L., Bachmann, B. O., Gunsior, M., Townsend, C. A., and Solomon, E. I. (2001) Spectroscopic studies of substrate interactions with clavaminate synthase 2, a multifunctional α-KG-dependent non-heme iron enzyme: Correlation with mechanisms and reactivities, *J. Am. Chem. Soc. 123*, 7388−7398.
32. Ho, R. Y. N., Mehn, M. P., Hegg, E. L., Liu, A., Ryle, M. A., Hausinger, R. P., and Que, L., Jr. (2001) Resonance Raman studies of the iron(II)-α-keto acid chromophore in model and enzyme complexes, *J. Am. Chem. Soc. 123*, 5022−5029.
33. Elkins, J. M., Ryle, M. J., Clifton, I. J., Dunning Hotopp, J. C., Lloyd, J. S., Burzlaff, N. I., Baldwin, J. E., Hausinger, R. P., and Roach, P. L. (2002) X-ray crystal structure of *Escherichia coli* taurine/α-ketoglutarate dioxygenase complexed to ferrous iron and substrates, *Biochemistry 41*, 5185−5192.
34. O'Brien, J. R., Schuller, D. J., Yang, V. S., Dillard, B. D., and Lanzilotta, W. N. (2003) Substrate-induced conformational changes in *Escherichia coli* taurine/α-ketoglutarate dioxygenase and insight into the oligomeric structure, *Biochemistry 42*, 5547−5554.
35. Brown, C. A., Pavlosky, M. A., Westre, T. E., Zhang, Y., Hedman, B., Hodgson, K. O., and Solomon, E. I. (1995) Spectroscopic and Theoretical Description of the Electronic Structure of S=3/2 Iron-Nitrosyl Complexes and Their Relation to O_2 Activation by Non-Heme Iron Enzyme Active Sites, *J. Am. Chem. Soc. 117*, 715−732.
36. Hegg, E. L., Whiting, A. K., Saari, R. E., McCracken, J., Hausinger, R. P., and Que, L., Jr. (1999) Herbicide-degrading α-keto acid-dependent enzyme TfdA: Metal coordination environment and mechanistic insights, *Biochemistry 38*, 16714−16726.
37. Gemperle, C., Aebli, G., Schweiger, A., and Ernst, R. R. (1990) Phase Cycling in Pulse EPR, *J. Magn. Reson. 88*, 241−256.
38. Mims, W. B., Davis, J. L., and Peisach, J. (1984) The Accessibility of Type I Cu(II) Centers in Laccase, Azurin and Stellacyanin to Exchangeable Hydrogen and Ambient Water, *Biophys. J. 45*, 755−766.
39. Schweiger, A., and Jeschke, G. (2001) *Principles of Pulse Electron Paramagnetic Resonance*, Oxford University Press, New York.
40. Mims, W. B. (1972) Amplitudes of Superhyperfine Frequencies Displayed in the Electron Spon Echo Envelope, *Phys. Rev. B 6*, 3543−3545.
41. Mims, W. B. (1972) Envelope Modulation in Spin-Echo Experiments, *Phys. Rev. B 5*, 2409−2419.
42. Hoffman, B. M., Venters, R. A., and Martinsen, J. (1985) General Theory of Polycrystalline ENDOR Patterns, *J. Magn. Reson. 62*, 537−542.
43. Cornelius, J. B., McCracken, J., Clarkson, R. B., Belford, R. L., and Peisach, J. (1990) Electron Spin Echo Envelope Modulation Angle Selection Studies of Axial Pyridine Coordination to Copper-(II) Benzoylacetonate, *J. Phys. Chem. 94*, 6977−6982.
44. Warncke, K., and McCracken, J. (1994) ^{2}H Electron Spin Echo Envelope Modulation Spectroscopy of Strong α-Hydrogen Hyperfine Coupling in Randomly-oriented Paramagnetic Systems, *J. Chem. Phys. 101*, 1832−1841.
45. Tyryshkin, A. M., Dikanov, S. A., and Goldfarb, D. (1993) Sum Combination Harmonics in Four-Pulse ESEEM Spectra. Study of the Ligand Geometry in Aqua-Vanadyl Complexes in Polycrystalline and Glass Matrices, *J. Magn. Reson., Ser. A 105*, 271−283.
46. Raitsimring, A. M., Pacheco, A., and Enemark, J. H. (1998) ESEEM Investigations of the High pH and Low pH Forms of Chicken Liver Sulfite Oxidase, *J. Am. Chem. Soc. 120*, 11263−11278.
47. Edmonds, D. T. (1977) Nuclear Quadrupole Double Resonance, *Phys. Rep. 29*, 233−290.
48. Yang, T. C., Wolfe, M. D., Neibergall, M. B., Mekmouche, Y., Lipscomb, J. D., and Hoffman, B. M. (2003) Substrate Binding to NO-Ferro-Napthalene 1,2 Dioxygenase Studied by High Resolution Q-Band Pulsed ^{2}H-ENDOR Spectroscopy, *J. Am. Chem. Soc. 125*, 7056−7066.
49. Hutchison, C. A., and McKay, D. B. (1977) The determination of hydrogen coordinates in lanthanum nicotinate dihydrate crystals by Nd+3-proton double resonance, *J. Chem. Phys. 66*, 3311−3330.
50. Silver, B. L. (1976) *Irreducible Tensor Methods*, Vol. 36, Academic Press, New York.
51. Dikanov, S. A., and Tsvetkov, Y. D. (1992) *Electron Spin Echo Envelope Modulation Spectroscopy*, CRC Press, Boca Raton, FL.
52. Arciero, D. M., Orville, A. M., and Lipscomb, J. D. (1985) ^{17}O-water and nitric oxide binding by protocatechuate 4,5-dioxygenase and catechol 2,3-dioxygenase, *J. Biol. Chem. 260*, 14035−14044.
53. Karlsson, A., Parales, J. V., Parales, R. E., Gibson, D. T., Eklund, H., and Ramaswamy, S. (2003) Crystal Structure of Napthalene Dioxygenase: Side-On Binding of Dioxygen to Iron, *Science 299*, 1039−1042.

BI700562T